Ultrafast spectroscopy and control of correlated quantum materials

By

Bryan T. Fichera

B.S., University of Pennsylvania (2017)

Submitted to the Department of Physics
in partial fulfillment of the requirements for the degree of

Doctor of Philosophy

at the

MASSACHUSETTS INSTUTITE OF TECHNOLOGY

May 2024

Authored by: Bryan T. Fichera
Department of Physics
May?, 2024

Certified by: Nuh Gedik
Donner Professor of Physics, Thesis supervisor

Accepted by: ?
? Professor of ?
? Chair of ?

Abstract

Lorem ipsum dolor sit amet, consectetuer adipiscing elit. Etiam lobortis facilisis sem. Nullam nec mi et neque pharetra sollicitudin. Praesent imperdiet mi nec ante. Donec ullamcorper, felis non sodales commodo, lectus velit ultrices augue, a dignissim nibh lectus placerat pede. Vivamus nunc nunc, molestie ut, ultricies vel, semper in, velit. Ut porttitor. Praesent in sapien. Lorem ipsum dolor sit amet, consectetuer adipiscing elit. Duis fringilla tristique neque. Sed interdum libero ut metus. Pellentesque placerat. Nam rutrum augue a leo. Morbi sed elit sit amet ante lobortis sollicitudin. Praesent blandit blandit mauris. Praesent lectus tellus, aliquet aliquam, luctus a, egestas a, turpis. Mauris lacinia lorem sit amet ipsum. Nunc quis urna dictum turpis accumsan semper.

Acknowledgements

Preface

The physics of solids is, to me, one of the most important and fundamental fields of modern science. This might seem, to some, a bit of a hot take. After all, by studying condensed matter physics, one learns next to nothing about, say, the formation of the stars and planets, or the origin of the universe. Nor does one learn about life, death, consciousness, disease, ethics, God, or any other question that perhaps puzzled humanity prior to about five hundred years ago. Certainly no one would argue that condensed matter physics is quite *useless*, given that nearly every device we interact with in modern life required some condensed matter physicist somewhere along the way to make one brilliant discovery or another – yet when the human mind starts to wander, and our thoughts turn to the metaphysical, we tend to look up, not down.

In my work I have taken a quite different view. Condensed matter physics, to me, is ultimately the study of how *truly boring* objects, when brought together in large quantites, *become* interesting, seemingly in spite of themselves. When electrons are put together in a lattice and allowed to interact slightly with the massive nuclei, at low enough temperatures they pair, the low-energy excitations become gapped, and current can flow for infinite times and with absolutely zero energy loss. Those same electrons, with some other set of interactions, may instead ionize (the opposite of pairing!) to create an electrically insulating state, whose low-energy excitation spectrum is nevertheless gapless and consisting of charge-neutral spin-$1/2$ particles. In all such cases, these systems exist in otherwise ordinary-looking rocks, fit in the palm of a hand[1], and are more or less indistinguishable from something you might find sticking into the bottom of your shoe.

While such systems may not tell us a lot[2] about the early universe, considering these and related problems lets us ask deep, fundamental questions about the world we live in – like, why is this thing a metal, but this thing is an insulator? What do those terms even mean? – that I don't think we would try to ask otherwise. To me, focusing our attention on

[1] Hopefully, gloved.

[2] This discussion is obviously intentionally reductive. In truth there is still quite a bit one can learn about, e.g. the early universe by studying condensed matter physics, see the Kibble and Pickett [13].

these problems, despite their obviously terrestrial nature, is not a waste of time; rather, I think they remind us that even the most mundane aspects of the human experience involve a level of complexity far beyond what we are capable of understanding absent the pursuit of science.

Throughout the seven years of my Ph.D., I hope to have made a few contributions to this pursuit. As the title of this work implies, I have mainly focused on the application of ultrafast techniques to the study of correlated quantum materials, which I loosely define as those materials in which the interaction between particles is large enough so as to compete with the kinetic energy of those particles. It is in these materials that I think lies the true frontier of condensed matter physics; here, much of our basic intuition about non- or weakly-interacting theory fails, and more complicated notions of phase competition, phase separation, disorder, pairing, coherence, etc. are needed to property describe the relevant physics.

In my own view, and in the view of many scientists in this field[1], the main question for strongly correlated physics amounts to: "Given a correlated system with some defined combination of different interaction strengths, is there a general theory which allows us to predict the phase diagram of this system *a priori*?" Related of course are questions about the origins of high-T_c superconductivity, strange metallicity, quantum spin liquids, and other exotic phases that we find emerging from strongly interacting systems. Since such a theory does not currently exist, at least with the level of predictive power that I think most would find satisfactory, new advances in this field typically come directly from experiment. Ultrafast optics plays a special role in this regard, for reasons that I will explain in chapter 1.

Progress thus happens in this field somewhat unsystematically, with small pieces of the puzzle added at random, but not infrequenct, intervals. Usually it is either new techniques or new materials that are the driving force here. To this end, I have tried to pursue both directions in my Ph.D. Appearing also in chapter 1 is thus a description of the materials I studied the most during my thesis, two of them, $CuBr_2$ and $CaMn_2Bi_2$ I consider criminally understudied. On the technique side, almost all of the work presented in this thesis was done using time-resolved second harmonic generation (tr-SHG), a relatively new, nonlinear optical technique which, at the most basic level, probes the point group assumed by the charge distribution function $\rho(\boldsymbol{x})$ at any given

point in time. Second harmonic generation (SHG) and tr-SHG are tricky techniques, with many pitfalls both practically and theoretically; chapters 2 and 3 are thus devoted to what I hope is a useful, if not fully compehensive, description of the technique. Chapter 4 is devoted to work that we did developing a new way to control the polarization of the light in a tr-SHG experiment using stepper motors. My hope is that these chapters are useful not only for the new student trying to build their own setup or analyze their own SHG data, but also for people for whom SHG is not a focus but nevertheless want to learn about it in slightly more detail than one would get from a typical paper or review article.

What follows, then, is a description of the three main research works I contributed during my Ph.D.. The first, which I describe in chapter 5, involves work that I did during my second and third years on $1T$-TaS_2, a very interesting charge density wave (CDW) material that, among other things, undergoes a mirror symmetry breaking CDW transition at $350\ \mathrm{K}$ that shows up in the SHG as a sudden distortion of the flower pattern at that temperature. Since this transition breaks mirror symmetry, two energetically degenerate domains should be present, corresponding to two opposite planar chiralities; in this work, we showed that SHG could differentiate between these two domains (i.e. the flower pattern in either domain looks different).

The second and third works, which I describe in chapters 6 and 7, in contrast to the $1T$-TaS_2work, both involve taking the system out of equilibrium to study the dynamics. In $CaMn_2Bi_2$ (chapter 6), we discovered that photoexcitation causes the antiferromagnetic (AFM) order in that compound to reorient (relative to equilibrium) to a metastable state which is impossible to reach from the equilibrium state thermodynamically. Light is thus used to *control* the magnetic order in this material.

In $CuBr_2$ (chapter 7), light is not used to control the order parameter like in $CaMn_2Bi_2$, but it does excite coherent oscillations of the collective modes of the multiferroic order (electromagnons), whose frequency, amplitude, damping, etc. may be probed in tr-SHG as a function of temperature – a methodology referred to as ultrafast *spectroscopy*. In doing so, we found that one of these collective modes is actually quite special, as it is in fact the analogue of the Higgs mode of particle physics in the context of a multiferroic material.

I conclude with various remarks in chapter 8, as well as an appendix, in which I enumerate briefly all of the null-result experiments I performed

during my Ph.D., in the hopes that future scientists don't have to waste time on what we already know are fruitless pursuits. If you have any questions about this or any other section of this thesis, please do not hesitate to reach out via email.

Contents

List of Figures

List of Tables

Chapter One

Ultrafast optics in correlated electron systems

Chapter Two

Second harmonic generation: theory

2.1 Space groups, point groups, and Neumann's principle

The utility of SHG in studying condensed matter systems is derived from the following simple statement, attributed to Franz Neumann[20] and later Pierre Curie[8]:

Theorem 2.1.1 (Neumann's principle) *Let P_G be the symmetry group of a crystal structure and P_H the symmetry group of some physical property of that crystal. Then, P_G is a subgroup of P_H.*

There are a few things to digest here. Let us start by understanding the meaning of the phrase "symmetry group". For any given crystal, there exists some infinitely large set of operations G under which the crystal structure is symmetric. Each of these operations may be decomposed into two parts: a "point-preserving operation" R, corresponding to either the identity, rotation, inversion, mirror, or the product of mirror and rotation, followed by a translation by some vector $\boldsymbol{\tau}$:

$$G = \{(R|\boldsymbol{\tau})\} \tag{2.1}$$

where $(R|\boldsymbol{\tau})$ means "Perform R, then translate by $\boldsymbol{\tau}$". Clearly, the set G forms a group, since if both g_1 and $g_2 \in G$ leave the crystal structure

invariant, so does the product $g_1 g_2$, and so $g_1 g_2 \in G$. Thus, G is called the *space group* of the crystal. In three dimensions, there are 230 crystallographic space groups, which are tabulated in a number of places, most usefully Wikipedia[6].

For 73 of these groups, the translation parts of the $\boldsymbol{\tau}$'s in eq. (2.1) are only ever linear combinations of integer multiples of the lattice vectors $\boldsymbol{a}$, $\boldsymbol{b}$, and $\boldsymbol{c}$; these are called *symmorphic* space groups. The remaining 157 groups involve translations that are not integer multiples of the lattice vectors; these are one's screw axes and glide planes, and so these groups are called *asymmorphic*.

Importantly, the "physical properties" of theorem 2.1.1 refer to the truly macroscopic properties of the crystal, like its conductivity, dielectric, or pyroelectric tensors. Consider, for example, that in SHG, we are typically studying the sample at optical wavelengths, where the wavelength of light is three or four orders of magnitude larger than the lattice spacing. Clearly, then, these properties do not care whether the correct symmetry is $(R|\boldsymbol{\tau})$ or $(R|\boldsymbol{\tau} + \boldsymbol{a}/2)$. A more useful group, then, is the *point group* of the crystal

$$P_G = \{R \text{ s.t. } \exists\, \boldsymbol{\tau} \text{ s.t. } (R|\boldsymbol{\tau}) \in G\} \tag{2.2}$$

i.e., the point group is the set of point-preserving operations R for which R appears in G, regardless of whether you need to perform a translation with it. Once can show that P_G is also a group, and thus it is P_G which is involved in Neumann's principle for all intents and purposes[1].

The last ingredient that we need to understand theorem 2.1.1 is the concept of what is meant by "physical propery". The idea is that the response of the crystal $J_{i_1 i_2 \cdots i_n}$ (i.e., the current J_i, or the quadrupole moment Q_{ij}) is proportional to some field $F_{i'_1 i'_2 \cdots 1'_m}$ via some tensor χ:

$$J_{i_1 i_2 \cdots i_n} = \chi_{i_1 i_2 \cdots i_n i'_1 i'_2 \cdots i'_m} F_{i'_1 i'_2 \cdots 1'_m}. \tag{2.3}$$

For example, the conductivity σ_{ij} relates a current density J_i to an applied electric field E_j:

$$J_i = \sigma_{ij} E_j. \tag{2.4}$$

[1] Of course this breaks down when the wavelength of light is comparable to the lattice spacing; in that case you need to consider the full space group.

Likewise, the polarization P_i due to the pyroelectric effect is related to the a temperature difference ΔT by a tensor p_i:

$$P_i = p_i \Delta T. \tag{2.5}$$

The tensors σ_{ij}, p_i, and generally, $\chi_{i_1 i_2 \cdots 1_n i'_1 i'_2 \cdots i'_m}$ are commonly referred to as *matter tensors*[25], to emphasize the fact that they are the only part of the response equations that depend on the material. It should be noted that matter tensors generically come in two types: those that transform like a vector under inversion and those that transform like a pseudovector under inversion. You can tell which is which by applying inversion to either side of the response equation. For example, the tensor ϵ_{ij} relating the displacement field to the electric field

$$D_i = \epsilon_{ij} E_j \tag{2.6}$$

is a polar tensor, whereas the tensor χ_{ij}^{me} describing the magnetoelectric effect

$$M_i = \chi_{ij}^{me} E_j \tag{2.7}$$

is an axial tensor.

We are now ready to restate theorem 2.1.1 in a slightly more useful form, using the terminology we have developed about point groups and matter tensors:

Theorem 2.1.2 (Neumann's principle, restated) *Let P_G be the point group of a given crystal, and let χ be a matter tensor describing some response function of that crystal. Then, for all $g \in P_G$, we have*

$$g(\chi) = \chi. \tag{2.8}$$

Equation (2.8) can be more usefully expressed if we know the matrix R_{ij}^g corresponding to g. For example, if g is "threefold rotation about the z axis", we have

$$R_{ij}^g = \begin{pmatrix} -\frac{1}{2} & -\frac{\sqrt{3}}{2} & 0 \\ \frac{\sqrt{3}}{2} & -\frac{1}{2} & 0 \\ 0 & 0 & 1 \end{pmatrix}, \tag{2.9}$$

in which case one can show that eq. (2.8) reads

$$(\det R^g)^t R_{i_1 i'_1}^g R_{i_2 i'_2}^g \cdots R_{i_n i'_n}^g \chi_{i'_1 i'_2 \cdots i'_n} = \chi_{i_1 i_2 \cdots i_n}, \tag{2.10}$$

where t is 0 if χ is a polar tensor and 1 if χ is an axial tensor. Theorem 2.1.2 tells us that there is one copy of eq. (2.10) for each $g \in P_G$.

Apparently, each element $g \in P_G$ gives us a *constraint* on the numbers $\chi_{i_1 i_2 \cdots i_n}$, in that they have to satisfy eq. (2.10). This is a remarkably useful fact. Since different point groups enforce different constraints on χ, that means the *form* of χ (e.g. when written as a list of numbers) depends quite sensitively on the point group of the crystal we are studying. As an example, here is the dielectric permittivity tensor for crystals with the point group (in Schoenflies notation) C_2:

$$\epsilon_{ij} = \begin{pmatrix} a & 0 & e \\ 0 & b & 0 \\ e & 0 & c \end{pmatrix}_{ij} \tag{2.11}$$

versus in the point group D_{3d}:

$$\epsilon_{ij} = \begin{pmatrix} a & 0 & 0 \\ 0 & a & 0 \\ 0 & 0 & c \end{pmatrix}_{ij} . \tag{2.12}$$

Clearly, any *measurement* of ϵ_{ij} will be able to easily differentiate a crystal with point group C_2 from one with point group D_{3d}. This is the fundamental basis, then, for SHG. In SHG, we measure the tensor χ_{ijk} corresponding to the response equation[2]

$$P_i(2\omega) = \chi_{ijk} E_j(\omega) E_k(\omega); \tag{2.13}$$

the numbers χ_{ijk} thus tell us about the crystallographic point group we are measuring from.

There are a couple of advantages to measuring χ_{ijk} over any other matter tensor in a given system. For one thing, χ_{ijk} is a third rank tensor, which means it has a few more degrees of freedom to work with compared to ϵ_{ij}, and thus does a better job at uniquely specifying each point group. It also doesn't have *too many* degrees of freedom, so that most of the time your experiment will be able to tell you all of your tensor elements[3]. In addition, since we are typically doing SHG at optical

[2]This discussion is a bit simplified in the sense that there are actually *many* response functions which will give you light at 2ω; for a more detailed discussion, see section 2.2.

[3]Quadrupole SHG has this problem, see section 2.2.

wavelengths, the form of χ_{ijk} reflects the symmetry of the *charge distribution* $\rho(\boldsymbol{x})$, in contrast to e.g. x-ray diffraction, where the relevant tensors will tell instead you about the electron distribution, $n(\boldsymbol{x})$. This can be advantageous in cases where the long range order you are trying to study involves an ordering of the valence electrons but not the electrons in the cores of atoms. This is entirely the result of the fact that Neumann's principle, as expressed both in theorem 2.1.1 and theorem 2.1.2, tells us that the point group of our crystal is a *subgroup* of the point group we get from our measurement – the measurement can always be more symmetric than the crystal!

As another example of this fact, let us note that the response equation given by eq. (2.13) clearly has an additional symmetry $j \leftrightarrow k$, since the two copies of the electric field on the right hand side are equivalent. Obviously this is not a result of the material we are studying, it is simply a fact of doing SHG. Thus, in addition to the constraints given by Neumann's principle and eq. (2.10), we have the additional constraint

$$\chi_{ijk} = \chi_{ikj} \forall i, j, k. \tag{2.14}$$

This is known as *particularization*[3].

2.2 A classical understanding of SHG

In the last section we considered the SHG response function given by eq. (2.13). Where does this relationship come from, and how is $P(2\omega)$ eventually measured? Our starting point in the classical treatment will be the inhomogenous electromagnetic wave equation

$$\left(\nabla^2 - \frac{1}{c^2}\frac{\partial^2}{\partial t^2}\right) E_i(\boldsymbol{x}, t) = S_i(\boldsymbol{x}, t), \tag{2.15}$$

which we understand as defining the field $E_i(\boldsymbol{x}, t)$ radiated by the source term $S_i(\boldsymbol{x}, t)$, which is induced by the incident field. To lowest order in a multipole expansion, $S_i(\boldsymbol{x}, t)$ is given by[12, 14]

$$\mu_0 \frac{\partial^2 P_i(\boldsymbol{x}, t)}{\partial t^2} + \mu_0 \left(\epsilon_{ijk} \nabla_j \frac{\partial M_k(\boldsymbol{x}, t)}{\partial t}\right) - \mu_0 \left(\nabla_j \frac{\partial^2 Q_{ij}(\boldsymbol{x}, t)}{\partial t^2}\right) \tag{2.16}$$

where $P_i(\boldsymbol{x}, t)$, $M_i(\boldsymbol{x}, t)$, and $Q_{ij}(\boldsymbol{x}, t)$ are the induced electric dipole, magnetic dipole, and electric quadrupole densities, and ϵ_{ijk} is the Levi-Civita tensor.

If the incident electric field is small, then the terms $P_i(\boldsymbol{x},t)$, $M_i(\boldsymbol{x},t)$, and $Q_{ij}(\boldsymbol{x},t)$ are linear functions of that electric field. However, for larger incident fields (such as those generated by pulsed lasers), they may be more generally written as a taylor series:

$$P_i = \chi^{ee}_{ij}E_j + \chi^{em}_{ij}H_j + \chi^{eee}_{ijk}E_jE_k + \chi^{eem}_{ijk}E_jH_k + \cdots \tag{2.17}$$
$$M_i = \chi^{me}_{ij}E_j + \chi^{mm}_{ij}H_j + \chi^{mee}_{ijk}E_jE_k + \chi^{mem}_{ijk}E_jH_k + \cdots \tag{2.18}$$
$$Q_{ij} = \chi^{qe}_{ijk}E_k + \chi^{qm}_{ijk}H_k + \chi^{qee}_{ijkl}E_kE_l + \chi^{qem}_{ijkl}E_kH_l + \cdots \tag{2.19}$$

where we have suppressed the arguments $\boldsymbol{x}$ and t for brevity.

Assuming the incident field is monochromatic,

$$E_i(\boldsymbol{x},t) = E_i(\omega)e^{i(\boldsymbol{k}\cdot\boldsymbol{x}-\omega t)} + \text{c.c.} \tag{2.20}$$
$$H_i(\boldsymbol{x},t) = H_i(\omega)e^{i(\boldsymbol{k}\cdot\boldsymbol{x}-\omega t)} + \text{c.c.} \tag{2.21}$$

the induced sources are also monochromatic, and (keeping only terms proportional to $e^{i2\omega t}$) we thus get

$$P_i(2\omega) = \chi^{eee}_{ijk}E_j(\omega)E_k(\omega) + \chi^{eem}_{ijk}E_j(\omega)H_k(\omega) \tag{2.22}$$
$$M_i(2\omega) = \chi^{mee}_{ijk}E_j(\omega)E_k(\omega) + \chi^{mem}_{ijk}E_j(\omega)H_k(\omega) \tag{2.23}$$
$$Q_{ij}(2\omega) = \chi^{qee}_{ijkl}E_k(\omega)E_l(\omega) + \chi^{qem}_{ijkl}E_k(\omega)H_l(\omega). \tag{2.24}$$

Since eq. (2.15) is linear, the electric field radiated by $S_i(\boldsymbol{x},t)$ is simply proportional to it. In the limit where the first term of eq. (2.22) dominates, the intensity measured at our detector thus satisfies

$$I(2\omega) \propto |\hat{e}^{\text{out}}_i \chi^{eee}_{ijk} \hat{e}^{\text{in}}_j \hat{e}^{\text{in}}_k|^2, \tag{2.25}$$

where $\hat{\boldsymbol{e}}^{\text{in}}$ and $\hat{\boldsymbol{e}}^{\text{out}}$ are unit vectors in the direction of the incoming and measured electric fields[4]. χ^{eee}_{ijk} does typically dominate when inversion symmetry is broken, but if not, you have to consider all of the terms in eqs. (2.22) to (2.24). Actually, each of these terms needs to be considered twice, since there is both a surface contribution and a bulk contribution[5]. In my experience, the heirarchy of contributions (from most to least important, and assuming everything is allowed by symmetry) is typically:

[4] Usually there are polarizers in the experiment which define these directions.

[5] The space group which constrains the surface contributions is the bulk space group less the operations which involve some change in the z coordinate.

1. Bulk electric dipole
2. Surface electric dipole, bulk electric quadrupole, and bulk magnetic dipole, at the same order[6]
3. Everything else

I've never seen anything outside of items 1 and 2, but in rare cases an electronic resonance may cause an enhancement in one of the other contributions[10].

Let us take a moment now to emphasize the following extremely common misconception about SHG: just because you see SHG in your experiment, that does not mean that inversion symmetry is broken in your material! It also does not mean that your material is a ferroelectric, or really that there's anything special at all about your material, at least before you've done any further analysis. Similarly, if you *don't* see SHG, that doesn't mean inversion symmetry is preserved, either. I have repeatedly seen large electric quadrupole SHG show up in materials with inversion symmetry, while materials which definitely break inversion symmetry have absolutely zero SHG observable in the experiment. The reason for this is ultimately due to resonance, a topic which I will discuss in section 2.3, but I mention it here because it is truly quite common in the literature and it is surely a mistake worth avoiding. You are "allowed" to say your material breaks inversion symmetry only if there is no other contribution in eqs. (2.22) to (2.24) which fits your data, and you are basically never allowed to say that your material preserves inversion symmetry when there is no SHG (a fact that should be obvious on a careful reading of theorem 2.1.1).

2.3 SHG in quantum mechanics

The description of SHG in the previous section is probably the most useful for understanding SHG from an "optics" perspective, but it gives little insight into the true microscopic origin of the SHG intensity. The quantum description, on the other hand, will tell you exactly where the SHG

[6]Somehow the bulk electric quadrupole and magnetic dipole contributions have been labelled "exotic" by some in the community, but that has not been my experience. If I had to guess, almost half of the materials I have measured with inversion symmetry show electric quadrupole SHG.

is coming from microscopically, but only if you have access to the eigenfunctions $|\psi\rangle$ of your hamiltonian – it is of little use otherwise. Nevertheless, we can still gain intuition about the dependence of our SHG intensity on the frequency of the light in the quantum picture, which will be useful for clearing up a whole other slew of misconceptions that have somehow made their way into the SHG literature. This treatment closely follows that of Boyd [4].

The starting point is to describe the system under study as a statistical ensemble specified by a Hamiltonian

$$H = H_0 + \lambda V \tag{2.26}$$

and a density matrix

$$\rho(t) = \sum_i p_i(t) \, |\psi_i(t)\rangle \, \langle\psi_i(t)| \tag{2.27}$$

where the $p_i(t)$'s specify the classical probability of the system being in state i at time t, and the $|\psi_i\rangle$'s are wavefunctions given by

$$|\psi_i(t)\rangle = \sum_n c_n^i(t) \, |n\rangle \tag{2.28}$$

for some $\{c_n^i(t)\}$, where

$$H_0 \, |n\rangle = E_n \, |n\rangle \tag{2.29}$$

for all n. In the presence of damping, the elements

$$\rho_{nm} = \langle\psi_n| \, \rho \, |\psi_m\rangle \tag{2.30}$$

of ρ satisfy the differential equation

$$\dot{\rho_{nm}} = \frac{1}{i\hbar}[H, \rho]_{nm} - \gamma_{nm}(\rho_{nm} - \rho_{nm}^{(\mathrm{eq})}), \tag{2.31}$$

where γ_{nm} is a matrix of (phenomenological) damping parameters[7], and $\rho_{nm}^{(\mathrm{eq})}$ is the density matrix corresponding to the equilibrium steady state of the system.

[7] This is just one choice of $p_i(t)$.

We consider the case where V may be treated as a perturbation on top of H_0, i.e. where λ is small. In this case, eq. (2.31) can be written

$$\dot{\rho}_{nm} = -i\omega_{nm}\rho_{nm} + \frac{1}{i\hbar}\sum_k \lambda(V_{nk}\rho_{km} - \rho_{nk}V_{km}) - \gamma_{nm}(\rho_{nm} - \rho_{nm}^{(\mathrm{eq})}), \quad (2.32)$$

where $\omega_{nm} = E_{nm}/\hbar$, and we seek a solution

$$\rho_{nm} = \rho_{nm}^{(0)} + \lambda\rho_{nm}^{(1)} + \lambda^2\rho_{nm}^{(2)} + \cdots . \quad (2.33)$$

Turning the crank (see Boyd [4] for details) gives us the solution

$$\rho_{nm}^{(N)}(t) = \int_{-\infty}^{t} \frac{1}{i\hbar}[\lambda V(t'), \rho^{(N-1)}(t')]_{nm} e^{(i\omega_{nm}+\gamma_{nm})(t'-t)}\, dt'. \quad (2.34)$$

Carrying out this series to second order in λ with the perturbation $V(t) = -\boldsymbol{\mu}\cdot\boldsymbol{E}(t)$, where $\boldsymbol{\mu}$ is the dipole moment and $\boldsymbol{E}(t) = \sum_q \boldsymbol{E}(\omega_q)e^{-i\omega_q t}$ is the incident electric field, we get an expression for the density matrix $\rho_{nm}^{(2)}(t)$ as a function of the dipole matrix elements

$$\boldsymbol{\mu}_{nm} = \langle n|\, \boldsymbol{\mu}\, |m\rangle\,, \quad (2.35)$$

the frequencies ω_q, the damping constants γ_{nm}, and $\rho_{nm}^{(0)}$.

Once we have $\rho_{nm}^{(2)}(t)$, we can compute the expectation value

$$\langle \boldsymbol{\mu}(t)\rangle = \sum_{nm} \rho_{nm}(t)\boldsymbol{\mu}_{nm}, \quad (2.36)$$

from which the susceptibility can be computed by taking two derivatives with respect to the electric field amplitudes[8]. Reproducing the final an-

[8] We are specializing here to the case of electric dipole SHG, although the calculation proceeds similarly for magnetic dipole and electric quadrupole.

swer here (again, from Boyd [4]):

$$\begin{aligned}\chi^{(2)}_{ijk}(\omega_p+\omega_q,\omega_q,\omega_p) = \frac{1}{2\epsilon_0\hbar^2}\sum_{lmn}(\rho^{(0)}_{ll}-\rho^{(0)}_{mm})\times\Bigg\{ \\ \frac{\mu^i_{ln}\mu^j_{nm}\mu^k_{ml}}{[(\omega_{nl}-\omega_p-\omega_q)-i\gamma_{nl}][(\omega_{ml}-\omega_p)-i\gamma_{ml}]} \\ +\frac{\mu^i_{ln}\mu^k_{nm}\mu^j_{ml}}{[(\omega_{nl}-\omega_p-\omega_q)-i\gamma_{nl}][(\omega_{ml}-\omega_q)-i\gamma_{ml}]} \\ +\frac{\mu^j_{ln}\mu^i_{nm}\mu^k_{ml}}{[(\omega_{nm}+\omega_p+\omega_q)+i\gamma_{nm}][(\omega_{ml}-\omega_p)-i\gamma_{ml}]} \\ +\frac{\mu^k_{ln}\mu^i_{nm}\mu^j_{ml}}{[(\omega_{nm}+\omega_p+\omega_q)+i\gamma_{nm}][(\omega_{ml}-\omega_q)-i\gamma_{ml}]} \\ \Bigg\},\end{aligned} \tag{2.37}$$

where $\omega_{nm} = \omega_n - \omega_m$. The SHG susceptibility tensor is then obtained by taking the limit $\omega_p = \omega_q$.

We learned two things by doing the quantum calculation. First of all, clearly if we know all of the eigenfunctions $|n\rangle$ of our unperturbed Hamiltonian, we can calculate the susceptibility tensor *a priori*, although this is obviously difficult except in the simplest of cases. Secondly, we notice that there are two types of denominators in eq. (2.37): those occuring at 2ω (remember we have set $\omega_q = \omega_p$) and those occuring at ω. Both can cause resonances in the SHG intensity and are observed abundantly in experiment[10]. The existence of resonances in the SHG spectrum makes comparison between different materials quite difficult if reference is made only to the SHG intensity at a single color. In one imfamous example, Wu et al. [34] incorrectly attributed the large SHG amplitude at optical wavelengths in TaAs to the presence of Weyl nodes near the Fermi level; later SHG spectroscopy measurements demonstrated that the enhancement was due to a simple band resonance at the excitation frequency used in that paper[22]. The emerging consensus is that the SHG intensity at optical frequencies has more or less nothing to do with the low-energy excitation spectrum or its topology.

2.4 SHG in the Ginzburg-Landau paradigm

While eq. (2.37) is quite general and completely correct microscopically, it obviously lends very little intuition into what kind of phenomenology we can expect to find in the SHG signal, say, across a phase transition, where the dipole matrix elements which determine eq. (2.37) certainly change but may not do so in a simple or straightforward way. An alternative approach is to treat SHG in a generalized Ginzburg-Landau paradigm, in which all of the physics of the system is cast in terms of an order parameter $\mathscr{O}_{i_1 i_2 \dots i_r}$. This approach was mainly developed by Sa et al. [28], based off of early work by Pershan [23] in the 1960s.

The key insight of Pershan is that one can define a "time-averaged free energy" in nonlinear optics by considering the term (assuming the incident field $E^{\text{in}}(t)$ is monochromatic with frequency ω)

$$F_{SHG} = -P_i(2\omega)E_i^{*\text{out}}(2\omega) + \text{c.c.} \tag{2.38}$$

$$= -[\chi_{ijk}E_i^{*\text{out}}(2\omega)E_j^{\text{in}}(\omega)E_k^{\text{in}}(\omega) + \text{c.c.}]. \tag{2.39}$$

Since F is a free energy, it must be a real, totally symmetric scalar, and eq. (2.39) thus gives us a way to *derive* the form of the tensor χ_{ijk} in a particular point group using similar arguments as in section 2.1.

In the context of a (spontaneous) symmetry-breaking transition at T_c, the Ginzburg Landau paradigm asserts that the free energy of eq. (2.39) still obeys the symmetry group of the high temperature phase, even though the low temperature phase explicitly breaks some of those symmetries. This is because the spontaneous symmetry breaking is considered a property of the *solution* of the free energy minimization problem, rather than a property of the minimization problem itself. Thus, a valid expression for the free energy in the low temperature phase is given by

$$F = -[\chi_{ijkl_1l_2\cdots l_r}(T > T_c)E_i^{*\text{out}}(2\omega)E_j^{\text{in}}(\omega)E_k^{\text{in}}(\omega) + \text{c.c.}]\mathscr{O}_{l_1l_2\cdots l_r}. \tag{2.40}$$

Comparing eqs. (2.39) and (2.40), we have an equation for the SHG susceptibility tensor in the low temperature phase

$$\chi_{ijk}(T < T_c) = \chi_{ijkl_1l_2\cdots l_r}(T > T_c)\mathscr{O}_{l_1l_2\cdots l_r}. \tag{2.41}$$

In light of eq. (2.41), let us consider the consequences of the symmetry of $\mathscr{O}$ on the SHG signal. For simplicity, let us consider a situation

that resembles a ferroelectric phase transition; i.e., the high temperature phase preserves inversion symmetry, but the low temperature phase involves the emergence of a rank-1 order parameter $\mathscr{O}_l$ which is odd under inversion. In that case, we have

$$\chi_{ijk}(T < T_c) = \chi_{ijkl}(T > T_c)\mathscr{O}_l(T), \tag{2.42}$$

i.e. the SHG at low temperature is simply a product of a high-temperature tensor and the order parameter $\mathscr{O}$. We of course need to check that χ_{ijkl} is allowed in the high temperature phase; here, we need χ_{ijkl} to be an even rank polar tensor, which is allowed in the presence of inversion symmetry (see eq. (2.10)).

Let us now imagine that the polarization $\mathscr{O}_l$ is known to be directed along the y axis, i.e.

$$\mathscr{O}_l = (0, P_0, 0)_l, \tag{2.43}$$

for some P_0. Then, by eq. (2.42), we have

$$\chi_{ijk}(T < T_c) = \chi_{ijky}(T > T_c)P_0. \tag{2.44}$$

Besides telling us that the susceptibility tensor is linear in the polarization magnitude P_0, what this formulation gets us is also that the elements of χ_{ijk} are just the elements of χ_{ijkl} with $l = y$. In many cases this is more information than you would have if you only knew the point group of the low temperature phase!

Equation (2.41) is also quite useful in the case where the low temperature phase is heterogenous; i.e. the order parameter $\mathscr{O}$ varies spatially from one point to another. This is commonly the case in magnets, for example, where rotational symmetry is spontaneously broken at T_c and the low temperature free energy thus consists of multiple energetically degenerate states related to each other by elements R of the high temperature point group which are broken at low temperature. These states have the same free energy since, again, the symmetry-breaking is due to to the order parameter, not due to the free energy itself. The order parameter in the different domains are thus related to each other via

$$\mathscr{O}_{i_1 i_2 \cdots i_r}(\boldsymbol{x}_1) = R[\mathscr{O}_{i_1 i_2 \cdots i_r}(\boldsymbol{x}_2)], \tag{2.45}$$

where the right hand side is given by eq. (2.10). Combining eq. (2.41) and eq. (2.45), the SHG tensor thus satisfies

$$\chi_{ijk}(\boldsymbol{x}_1) = R[\chi_{ijk}(\boldsymbol{x}_2)]. \tag{2.46}$$

Equation (2.46) is the fundamental basis for our SHG works on 1T-$TaS_2$and $CaMn_2Bi_2$, discussed in chapters chapter 5 and chapter 6.

Chapter Three

Second harmonic generation: practical

3.1 Description of the setup

In the last chapter we saw that the SHG intensity in a given crystal is related to the point group, order parameter, band structure, etc. of that crystal via the susceptibility tensor χ_{ijk}. It is also obvious from section 2.1 that the ideal scenario is to be able to measure as many of the numbers χ_{ijk} as possible; after all, if you only measured the xx component of eqs. (2.11) and (2.12), you would have obtained essentially no information about your crystal whatsoever. The SHG setup that we built (whose design is mostly credited to Torchinsky and Hsieh[30], with some improvements by us which I will discuss below) was designed with exactly this goal in mind. There are two key insights which make this design work: one, the light is obliquely incident on the sample so there is some component of $\boldsymbol{E}^{\text{in}}$ directed along the sample normal, and two, we rotate the plane of incidence so that the in-plane field direction sweeps an entire 360°. The first point allows us to measure elements of χ_{ijk} with z indices[1], and the second point makes sure we get all of the x and y elements of χ_{ijk} too. All of the tensor elements are thus given a chance to contribute to the SHG intensity in a given experiment.

With those considerations in mind, let me proceed to give a schematic description of our SHG setup. Some of the choices we made may seem

[1]Here and unless otherwise noted I define the sample normal to be the z axis.

arbitrary right now, but I will go over them in detail in section 3.2. The starting point is our regenerative amplifier (Spectra-Physics Spitfire Sptf-100f-5k-xp), which produces 100 fs 800 nm pulses at a 5 kHz repetition rate from an 86 MHz seed laser (Spectra-Physics Tsunami 3941-M1S). 90% of the beam is split off to power an optical parametric amplifier (OPA), and the remaining 10% is used for the SHG probe beam. After passing through an optical telescope, which creates a collimated beam of width $1 - 2$ mm, this beam is attenuated with a polarizer - half-wave plate - polarizer triplet, and then elliptically polarized with a quarter-wave plate and half-wave plate in series. The ellipticity at this stage is set so the light is perfectly circularly polarized following transmission through a phase mask, as described below.

After passing through these polarization optics, the beam is focused with a lens onto the aforementioned phase mask, which acts as a transmissive diffraction grating and separates the beam into multiple different diffraction orders. The $+1$ order diffraction comes off at an angle of roughly $7°$, while the other orders are blocked with anodized aluminum foil. This (diverging) beam then propogates at $7°$ to the optical axis before meeting a lens set at the appropriate distance so as to both collimate the beam and rectify the $7°$ progation angle. Then, the light passes through a dichroic mirror (which transmits 800 nm and reflects 400 nm), becomes linearly polarized by a wire-grid polarizer, and is then focused onto the sample at a $10°$ angle of incidence by passing through the edge of a 1 in-diameter 50 mm achromatic focusing lens. The interaction between the light and the sample causes SHG to be radiated in reflection at the same $10°$ angle of incidence, so that the SHG beam passes through the opposite side of the 50 mm lens before passing through a second, independent polarizer which is used to control the polarization of the measured light.

Finally, the polarized output reflects off of two dichroic mirrors (oriented in such a way as to cancel the differing effect of the Fresnel equations on the reflectivity of S and P polarized light) and is focused through a 400 nm bandpass filter onto a photomultiplier tube (PMT) by a 400 mm lens. The current output of the PMT is filtered by a lock-in amplifier (for static SHG, set to the 5 kHz repetition rate of the laser) and read out on an oscilloscope. The phase mask, incoming polarizer, and outgoing polarizer are mounted on rotating lens tubes which are connected via pulley to a common motor shaft driven at ~ 5 Hz by a brushless DC motor. The motor thus continuously rotates the plane of incidence of the experiment,

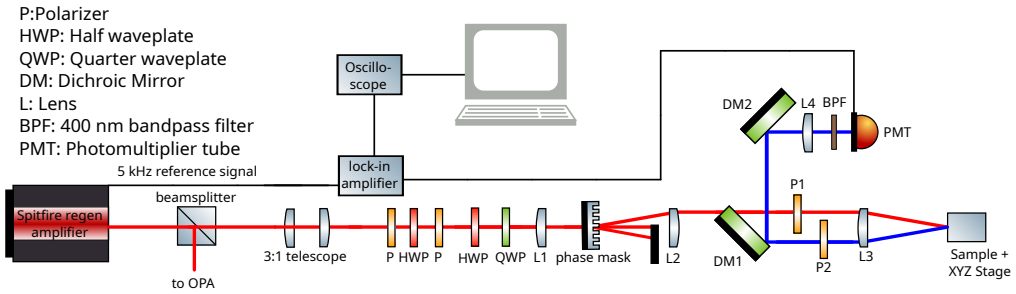

Figure 3.1: Schematic drawing of the SHG setup used in this research. After Morey et al. [18].

since the latter is entirely defined by the phase mask and the polarizers. The rotation angle is tracked as a function of time by an optical rotary encoder, consisting of a laser pointer passed through a chopper wheel (with 100 slots) mounted at the end of the motor shaft and detected via photodiode. The encoder signal and the lock-in signal are both sent to a homemade oscilloscope (an Arduino Uno microcontroller which separates the lock-in signal into different individual rotations by looking for peaks in the encoder signal), the output of which is sent to a computer for further data processing.

3.2 Before you build

I list here a few essential aspects of SHG that should be considered before designing a new setup.

3.2.1 Spot size

One of the most important quantities in an SHG setup is the diameter of the probe spot. Ideally, this diameter is as small as possible, so as to measure the smallest samples or domain sizes. However, there is an important caveat: for constant fluence (i.e. supposing we are limited by the sample damage threshold), the SHG signal to noise ratio scales linearly in the area excited by the probe, and thus SHG microscopes have a difficult time measuring small SHG signals compared to traditional SHG setups with a larger excitation area. To see this, let us say that our detector mea-

sures the number of photons per SHG pulse, which is proportional to the pulse energy $U_p(2\omega)$. Assuming the input and output pulse intensity profiles have the shape of a square wave with width τ and height $I_p(\omega)$ and $I_p(2\omega)$, respectively, we have

$$U_p(2\omega) = AI_p(2\omega)\tau \tag{3.1}$$

and

$$U_p(\omega) = AI_p(\omega)\tau \tag{3.2}$$

where A is the area of the beam at the sample surface. The SHG intensity is proportional to the square of the input intensity

$$I_p(2\omega) \propto I_p^2(\omega) \tag{3.3}$$

so that

$$U_p(2\omega) \propto \frac{U_p^2(\omega)}{A\tau}. \tag{3.4}$$

Substituting for the fluence f

$$f(\omega) = \frac{U_p(\omega)}{A} \tag{3.5}$$

we have

$$U_p(2\omega) \propto \frac{f^2(\omega)A}{\tau} \tag{3.6}$$

i.e., if we hold the fluence constant at the sample damage threshold, the number of photons in the generated SHG pulse is proportional to the excitation area and inverse to the pulse width. The signal to noise ratio is then given by

$$\mathrm{SNR} \propto \frac{U_p(2\omega)}{\sqrt{r}} \tag{3.7}$$

where r is the system repetition rate.

3.2.2 Oblique vs. normal incidence

While all of the results presented in this thesis utilized the setup in fig. 3.1, where the incident beam makes a small angle with respect to the sample normal, plenty of groups use a different approach where that angle is set to $0°$. This has the obvious disadvantage of not specifying all of the tensor

elements, since any element χ_{ijk} with $i, j, k = z$ is not accessible in this geometry. However, in some cases this can actually be something of an advantage. For example, sometimes unwanted SHG contributions (see section 2.2) may be avoided in the normal incidence geometry, assuming the numerical aperture (NA) of the focusing optic is small enough that longitudinal components of the electric field are nearly zero. Furthermore, in some materials the order parameter only couples to one or two elements of χ_{ijk}; if none of these elements have a z index, it is needless to complicate the analysis with oblique incidence.

In my experience, oblique incidence seems to be useful in two broad cases. For one thing, some order parameters only show up in the z components of χ_{ijk} (this is the case in $1T$-TaS_2, see **??**), in which case one obviously needs a nonzero angle of incidence to access these components. A more subtle point is that, even if in practice all of the phenomenology of a particular sample only shows up in the x and y indices of χ_{ijk}, still one must measure the full tensor to *rule out* unseen phenomenology in the other indices. Both the $CaMn_2Bi_2$ (chapter 6) and $CuBr_2$ (chapter 7) works presented in this thesis are examples of exactly this point, where the main scientific arguments involve either comparing SHG patterns in two domains or comparing oscillation amplitudes in different polarization channels. Clearly one needs to know all of the tensor elements to make those arguments exact.

3.2.3 Choice of detector

Our setup is somewhat unique in using a PMT for data collection rather than an electron multiplying charge coupled device (EM-CCD), which is the slightly more traditional method. Frankly, this decision was not based on the detection efficiency, but rather the fact that PMTs typically cost about two orders of magnitude less than EM-CCDs. However, the setup construction with a PMT is slightly different than with an EM-CCD, so you should probably decide which you want to use before you start building your setup. With an EM-CCD, the beam is sent into the device without focusing (L4 in fig. 3.1) so that the beam traces a circle on the sensor as a function of time[11]. The rotational anisotropy signal is read off by performing a radial integration of the camera image (after masking the part of the image which is outside from the circle traced by the beam). In this way, the rotation angle of the motor is correlated

with the SHG signal via the azimuthal degree of freedom on the camera image. In contrast, with a PMT the SHG signal is read out as a function of time on an oscilloscope (see section 3.1), and must be correlated with the rotation angle of the motor by some other method. We use an optical chopper wheel attached to the motor shaft; a beam from a laser pointer is directed through the chopper wheel and onto a photodiode, which produces a square wave signal that is used to trigger the oscilloscope. One must also be careful that the PMT is aligned as close to normal as possible to the axis defined by DM2 and L4 in fig. 3.1, as the PMT output is actually quite sensitive to the angle of incidence of the input radiation.

As for the detection efficiency of the two devies, an EM-CCD is basically an *array* of PMTs – thus, there is no fundamental difference in the detection efficiences of the two methods, although having never used an EM-CCD I cannot speak to any specific considerations that might favor one over the other.

3.3 tr-SHG: methodology

Polarization control

The main limitation for doing tr-SHG is simply that the experiment becomes longer. Each measurement of χ_{ijk} requires averaging four different polarization channels ($P_{\text{in}}P_{\text{out}}$, $P_{\text{in}}S_{\text{out}}$, $S_{\text{in}}P_{\text{out}}$, and $S_{\text{in}}S_{\text{out}}$), which, depending on the signal to noise ratio, can take as long as $2-3$ minutes each. In a time-resolved experiment, that procedure must be repeated at least once for each time delay; in fact, it us often useful to sweep the delay stage multiple times to reduce the extent to which systematic drifts in in the laser power, alignment, etc. affect the time trace. Not only is this time-consuming (typically taking ~ 12 hours to get a good dataset), but it also requires four rotations of the polarizers at each delay, which is simply not feasible if the polarizers are to be rotated manually. Unfortunately, automated polarizer rotation is difficult in the rotational anisotropy SHG (RA-SHG) experimental geometry because the polarizers must be rotated relative to a lens tube which is *itself* rotating at 5 Hz. The traditional method of rotating polarizers via stepper motor is thus not possible, unless one finds a method to transmit power between the stationary laboratory frame and the rotating frame that the polar-

izer lives in. Myself and Karna Morey designed such a method using an electronic device known as a hollow-bore electric slip ring, which uses ring-shaped conductive pads in combination with low-friction metallic brushes to conduct electricity between two rotating objects. In my opinion, such a design is essential to doing tr-SHG unless one is satisfied with only measuring a single polarization channel; thus, I have dedicated the entirety of chapter 4 to our solution, which in my opinion represents the largest contribution we made to SHG methodology during this thesis.

The pump beam path

Having discussed the modifications needed for tr-SHG on the probe arm, let us now describe the pump beam path. $100\ \mathrm{fs}$ pulses from the regenerative amplifier (Spectra-Physics Spitfire Sptf-100f-5k-xp) are split by $90:10$ beamsplitter (with the 10% becoming the probe beam, see section 3.1) and are used as input to an OPA (Light Conversion TP8F1N3) which produces light of variable wavelength between 1100 and $2080\ \mathrm{nm}$. The output of the OPA is directed through a wire-grid polarizer (to pick out the signal or idler, as needed) to an optical delay line (Newport DL125 with SMC100 motion controller) and a second polarizer to vary the beam power. The beam then passes through a NIR (near-infrared) longpass filter to remove unwanted visible wavelengths that are output by the OPA. A $400\ \mathrm{nm}$ lens focuses the beam past two mirrors (one mounted with epoxy onto the focusing lens L3 of fig. 3.1[2]) and finally onto the sample. The diameter of the pump beam at the focus is set by moving the lens position along the beampath and monitoring the beam shape with a CCD camera. The pointing of the beam is aligned so that the light reflected off the sample is perfectly backscattered. Pump scatter is avoided by mounting a small black circular disk in the center of L3, and by subtracting "dark" scans without the probe beam from the final dataset.

An optical chopper wheel is placed somewhere in the pump beam path which blocks every other pulse from the OPA, so that the effective repetition rate of the pump pulsetrain is $2.5\ \mathrm{kHz}$. The output of the PMT (see fig. 3.1) is sent to a lock-in amplifier synced to this frequency, so that

[2]Remember that the probe beam is arriving at oblique incidence and thus passes through the edge, rather than the center, of L3.

the output of the lock-in is proportional to

$$I^{\mathrm{SHG}}_{\mathrm{Pump+Probe}} - I^{\mathrm{SHG}}_{\mathrm{Probe}} \tag{3.8}$$

i.e. the output of the lock-in is the pump-induced change in the measured SHG intensity.

Finally, the pump-probe time delay is varied, and for each delay the rotational anisotropy in the SHG intensity is measured in each of the four polarization channels. Alternatively, the motor rotation may be parked at a fixed angle and the SHG intensity at this angle measured as a function of delay time.

3.4 Data analysis

Finally, we discuss the analysis of SHG data, first in the static limit and then in the context of tr-SHG.

3.4.1 Static RA-SHG patterns

The typical static RA-SHG dataset consists of a set of points $\{(\phi_n, I^p_n)\}$, $n \in \{0, 1, \ldots N-1\}$ and standard errors $\{\sigma^p_n\}$ for each of the four independent polarization channels

$$p \in \{P_{\mathrm{in}}P_{\mathrm{out}}, P_{\mathrm{in}}S_{\mathrm{out}}, S_{\mathrm{in}}P_{\mathrm{out}}, S_{\mathrm{in}}S_{\mathrm{out}}\}.$$

By eq. (2.13), each of these patterns may be modeled by an equation[3]

$$I^p(\phi) \propto |\hat{e}^{p,\mathrm{out}}_i(\phi)\chi_{ijk}\hat{e}^{p,\mathrm{in}}_j(\phi)\hat{e}^{p,\mathrm{in}}_k(\phi)|^2, \tag{3.9}$$

where $\hat{\boldsymbol{e}}$ is a unit vector in the direction of the corresponding electric field. These unit vectors are given as a function of ϕ and the angle of incidence θ in table 3.1.

[3] I will focus on electric dipole SHG for now, although note that the equations for electric quadrupole and magnetic dipole SHG (eqs. (2.23) and (2.24)) are different – by eq. (2.16), both involve a factor of the incident wavevector $\boldsymbol{k}$, and the magnetic dipole term has a cross product.

Table 3.1: Vector definition of polarization channels. θ is the angle of incidence and ϕ is the angle of the plane of incidence with respect to the $\hat{x}$ axis.

Input	Output	$\hat{\boldsymbol{e}}^{\text{in}}(\phi)$			$\hat{\boldsymbol{e}}^{\text{out}}(\phi)$		
		$\hat{e}_x^{\text{in}}(\phi)$	$\hat{e}_y^{\text{in}}(\phi)$	$\hat{e}_z^{\text{in}}(\phi)$	$\hat{e}_x^{\text{out}}(\phi)$	$\hat{e}_y^{\text{out}}(\phi)$	$\hat{e}_z^{\text{out}}(\phi)$
P	P	$\cos\phi\cos\theta$	$\sin\phi\cos\theta$	$-\sin\theta$	$-\cos\phi\cos\theta$	$-\sin\phi\cos\theta$	$-\sin\theta$
P	S	$\cos\phi\cos\theta$	$\sin\phi\cos\theta$	$-\sin\theta$	$-\sin\phi$	$\cos\phi$	0
S	P	$-\sin\phi$	$\cos\phi$	0	$-\cos\phi\cos\theta$	$-\sin\phi\cos\theta$	$-\sin\theta$
S	S	$-\sin\phi$	$\cos\phi$	0	$-\sin\phi$	$\cos\phi$	0

Let us assume that we know the point group P_G of our material. Then, the first step is to constrain the values of χ_{ijk} using the arguments of section 2.1. One can do this manually by solving the system of equations defined by eq. (2.10), or one can simply look up the answer in one of a number of tables (e.g. Boyd [4])[4]; in the end we are left with a tensor $\chi_{ijk}^{P_G}$ with M independent elements $\{\chi_i, i \in 0, 1, \ldots, M-1\}$.

The goal is to simultaneously fit the four patterns $\{(\phi_n, I_n^p\}$ to eq. (3.9) using the χ_i's. Our objective function is thus

$$f(\{\chi_i\}) = \sum_{\substack{p \in \{P_{\text{in}}P_{\text{out}}, P_{\text{in}}S_{\text{out}}, \\ S_{\text{in}}P_{\text{out}}, S_{\text{in}}S_{\text{out}}\}}} \sum_{n=0}^{N-1} \left(\frac{I^p(\phi_n) - I_n^p}{\sigma_n^p} \right)^2 \tag{3.10}$$

with $I^p(\phi)$ defined in eq. (3.9). Unfortunately, such a function is quite difficult to minimize. The reason is that $I^p(\phi)$ is ultimately a sum of products of trigonometric functions of ϕ (due to table 3.1) which can be difficult for typical minimization algorithms. An alternative is to cast the problem in terms of the Fourier transforms (FTs)

$$\hat{I}^p(k) \equiv \frac{1}{2\pi} \int_0^{2\pi} I^p(\phi) e^{-ik\phi} \, d\phi \tag{3.11}$$

of $I^p(\phi)$ and the discrete Fourier transforms (DFTs)

$$\{(k, \hat{I}_k^p)\}, \tag{3.12}$$

of $\{(\phi_n, I_n^p)\}$, where[5]

$$\hat{I}_k^p \equiv \frac{1}{N} \sum_{n=0}^{N-1} I_n^p e^{-ik\phi_n}. \tag{3.13}$$

Since the DFT is unitary, the uncertainties $\hat{\sigma}_k^p$ are simply the DFT of the σ_n^p's. Thus, our new objective function is

$$f(\{\chi_i\}) = \sum_{\substack{p \in \{P_{\text{in}}P_{\text{out}}, P_{\text{in}}S_{\text{out}}, \\ S_{\text{in}}P_{\text{out}}, S_{\text{in}}S_{\text{out}}\}}} \sum_{k=0}^{N-1} \left(\frac{\hat{I}^p(k) - \hat{I}_k^p}{\hat{\sigma}_k^p} \right)^2. \tag{3.14}$$

[4]Be aware that these tensors are given in just one of many choices of coordinates; a rotation of χ_{ijk} may be needed to agree with the orientation of the crystal in the experiment.

[5]I am assuming the ϕ_n's are equally spaced.

This is a much easier function to minimize for two reasons: one, the function is now just a quadratic function of the $\{\chi_i\}$'s, and two, since there are only six factors of trigonometric functions of ϕ in $I^p(\phi)$, $\hat{I}^p(k) = 0$ for $k \notin \{-6, -5, \ldots, 6\}$[6] (the other terms in eq. (3.14) just contribute an overall constant to f).

What is left then is just the choice of minimization algorithm. Unfortunately, simple gradient descent algorithms are not ideal here unless you have a really good initial guess, since eq. (3.11) is still quadratic in the fitting parameters and the global minimum is often surrounded by many local minima which can easily cause these algorithms to become trapped. Global minimization routines are thus optimal; I have used the simulated annealing algorithm of Xiang et al. [35] with success, as well as the related "basinhopping" algorithm of Wales and Doye [33], both of which are implemented in `scipy.optimize`[31]. Ultimately, though, it is up to the experimenter to ensure they have found the true global minimum of eq. (3.14).

As part of this thesis, I wrote a software package in Python called ShgPy which uses `sympy`[17] to compute the FT model eq. (3.11) and `scipy.optimize`[31] to fit this model to the data via eq. (3.14). Installation instructions and a comprehensive documentation may be found at the project home page `https://bfichera.github.io/shgpy/`.

3.4.2 Modeling χ_{ijk}: the simplified bond hyperpolarizability model

Sometimes the symmetry-constrained χ_{ijk} of section 3.4.1 is difficult to analyze (perhaps it has too many fitting parameters), in which case it might be prudent try and justify an even more tightly constrained χ_{ijk} via some a microscopic model. We have already seen two such models via eqs. (2.37) and (2.41), but the former is typically not tractable and the latter may only be valid in the presence of a spontaneous symmetry-breaking phase transition with a well-defined order parameter. One alternative is to model the microscopic charge degrees of freedom classically – suppose most of the motion of charges in our solid occurs in the bonds between atoms, and that that motion is constrained to occur along

[6] This is the case for electric dipole SHG; for electric quadrupole and magnetic dipole, we can have as much as $k = \pm 8$.

the bond direction only. Then, the solid can be modeled as an ensemble of oscillating dipoles (one for each bond in the unit cell) with corresponding hyperpolarizabilities $\{\alpha_n\}$. Symmetry may dictate how many independent α_n's there are in the unit cell, but otherwise these are considered unknown and to be fit to the data. The electric dipole SHG response of such an ensemble was analyzed by Powell et al. [24], and the electric quadrupole response was later considered by Bauer and Hingerl [2]; the answer in both cases is quite simple:

$$\chi^{eee}_{ijk} = \sum_n \alpha_n b^n_i b^n_j b^n_k \tag{3.15}$$

$$\chi^{qee}_{ijkl} = \sum_n \gamma_n b^n_i b^n_j b^n_k b^n_l \tag{3.16}$$

where $\boldsymbol{b}^n$ is a unit vector in the direction of bond n and the α_n's and γ_n's are the unknown parameters of the dipole and quadrupole models, respectively.

When valid, this simplified bond hyperpolarizability model (SBHM) is powerful for two reasons: for one, eqs. (3.15) and (3.16) typically have fewer unknown parameters than the naive, symmetry-constrained tensor $\chi^{P_G}_{ijk}$ of section 3.4.1, and two, there is a direct connection between the unknown parameters α_n and γ_n and the microscopic degrees of freedom. One can thus draw conclusions *about* the microscopic degrees of freedom by fitting the SHG patterns to eqs. (3.15) and (3.16) (see, e.g., Ron et al. [27]). Of course, one must be careful that the assumptions of this model – that the charges are localized to the bonds, and that the only relevant motion is along the bond direction – are actually correct before proceeding with this sort of analysis.

Myself and Karna Morey built a comprehensive interface to the SBHM in Python using `pymatgen`[21], which takes an arbitrary crystallographic information file (CIF) file and calculates the relevant susceptibility tensors via eqs. (3.15) and (3.16). The change to the susceptibility tensor induced by an elastic distortion mode ($\chi_{ijk}(q)$, where q is the mode amplitude) can be computed via integration with `ISODISTORT`[5, 29]. See the package documentation (`https://github.com/morey18k/sbhm.git`) for examples and further information.

3.4.3 Fitting time traces in tr-SHG

As the final section of this chapter, let me remark on a few aspects of fitting time-domain signals that are not necessarily specific to SHG, but are nevertheless essential for tr-SHG analysis.

Typically, in tr-SHG we plot the pump-induced change in the SHG intensity at a single angle ϕ_0 as a function of the delay time t; more complicated analysis of the tensor elements themselves is possible but often unnecessary. This intensity change $\Delta I_{2\omega}(t, \phi_0)$ is related to $P(2\omega)$ via

$$\begin{aligned} \Delta I_{2\omega}(t,\phi_0) &= I_{2\omega}^{\text{Pump+Probe}}(t,\phi_0) - I_{2\omega}^{\text{probe}}(0,\phi_0) && (3.17)\\ &\propto |P_{2\omega}(0,\phi_0) + \delta P_{2\omega}(t,\phi_0)|^2 - |P_{2\omega}(0,\phi_0)|^2 && (3.18)\\ &\propto 2P_{2\omega}(0,\phi_0)\delta P_{2\omega}(t,\phi_0) + |\delta P_{2\omega}(t,\phi_0)|^2 && (3.19) \end{aligned}$$

where we have used that the signal is presumably independent of time if there is no pump pulse. When $|\delta P_{2\omega}(t, \phi_0)| \ll |P_{2\omega}(0, \phi_0)|$, this reduces to

$$\Delta I_{2\omega}(t,\phi_0) \propto P_{2\omega}(0,\phi_0)\delta P_{2\omega}(t,\phi_0). \tag{3.20}$$

The basic problem is then that we have a dataset $\{t_n, I_n\}, n \in \{0, 1, \ldots, N-1\}$ with uncertainties σ_n which we wish to fit to some model, typically consisting of some (e.g. polynomial) background $b(t, \{b_k\}), k \in \{0, 1, \ldots, K-1\}$ plus 1 to M damped harmonic oscillators

$$I(t,\theta) = \begin{cases} 0 & t < 0 \\ b(t,\{b_k\}) + \sum_{m=1}^{M} A_m e^{-t/\tau_m}\cos(2\pi f_m t + \psi_m) & t > 0 \end{cases}, \tag{3.21}$$

where θ refers to the set of unknown parameters $\{b_k\}$, $\{A_m\}$, $\{\tau_m\}$, $\{f_m\}$, and $\{\psi_m\}$. We wish to determine the model coefficients θ by minimizing the objective function

$$f(\theta) = \sum_{n=0}^{N-1} \left(\frac{I(t_n,\theta) - I_n}{\sigma_n} \right)^2. \tag{3.22}$$

Various algorithms exist to find the minimum θ_0 of f; the Levenberg-Marquardt (LM) algorithm [15, 16] is known to have trouble with exponential functions, so it is recommended to do a Nelder-Mead search [19] first and then use LM to refine the solution. These methods also report the uncertainties $\{\sigma_i\}$ on each fitting parameter, basically by computing

the curvature of the function f near θ_0 (which depends, among other things, on the data uncertainty $\{\sigma_n\}$). Importantly, however, these uncertainties are only valid when f is a linear function of the model parameters near the minimum![7] This is a point which is completely overlooked in the ultrafast condensed matter literature, even though there is really no reason that eq. (3.22) should satisfy this criterion for typical uncertainty levels in pump-probe experiments.

The correct approach in this case is to note that the data set $D_0 \equiv \{t_n, I_n\}$ is just one of many possible datasets $D_0, D_1, D_2, \ldots$ that we *could* have measured during our experiment.[8] If we could run the minimization procedure described above for each of these hypothetical datasets, we would end up with a whole distribution of model coefficients $\theta_0, \theta_1, \theta_2, \ldots$ from which our measurement θ_0 was just a single draw. The spread of this distribution (or, more precisely, the spread of the distribution $\theta - \theta_{\text{true}}$) reflects exactly the quantitative uncertainty in our measurement of θ that we would like to report.

Our goal, then, is to approximate this distribution by some method. One approach (which works when we have many observations $\{t, I\}$ with the same t) is called the nonparametric bootstrap[7]. For each time t_n, let us say that we have a set of measured intensities $\{I_m^n\}$, with $m \in \{1, 2, \ldots, M_n\}$. Then, we generate new hypothetical datasets $\mathscr{D}_1, \mathscr{D}_2, \ldots$ by (for each t_n) drawing M_n items *with replacement* from the $\{I_m^n\}$'s. The fact that this new distribution of datasets is a faithful representation of the true distribution $\{D_0, D_1, D_2, \ldots\}$ is not obvious, but theoretical work by many authors (see Wackernagel [32] for a review) has established that it is nevertheless true.

If we are confident that our model $I(t, \theta)$ is, in fact, the true model (at least for some set of coefficients θ_{true}), then rather than using the dataset D_0 to generate our hypothetical datasets, we can instead choose to use the model *itself*. The idea is to take our estimate $I(t, \theta_0)$ and generate new datasets $\{\mathscr{D}_m\}$ essentially by adding noise:

$$\mathscr{D}_m = \{(t_n, I(t_n, \theta_0) + N_n), n \in \{0, 1, \ldots, N-1\}\}, \tag{3.23}$$

for some random variable N_n which we put in by hand. This is called the parametric bootstrap, referring to the fact that we are estimating

[7] Here, "near" means "in a neighborhood of size σ_i.

[8] The following discussion closely follows that of *Numerical Recipes*, chapter 15[26].

our true distribution $\{D_0, D_1, D_2, \ldots\}$ via the parameters θ_0[9]. In order for the distribution of $\mathscr{D}_m$'s to faithfully represent the true distribution $\{D_0, D_1, D_2, \ldots\}$, obviously N_n needs to reflect the actual noise distribution of the experiment. Thankfully, in pump-probe experiments, we usually know this distribution – as long as we have enough points (t_n, I_n) with $t_n < 0$, we can estimate N_n with a normal distribution centered about 0 with variance $\langle (I_n)^2 \rangle_{<0} - \langle I_n \rangle_{<0}^2$, where $\langle \cdot \rangle_{<0}$ means "average over points with $t_n < 0$."

Once we have the hypothetical datasets $\{\mathscr{D}_m\}$, we proceed by estimating a θ_m for each one (using eq. (3.22)), and then plotting the distribution $\{\theta_m - \theta_0\}$; the spread of this distribution tells us the uncertainties σ_i in each of our model coefficients. These uncertainties are much more reflective of the true uncertainty in our measurement of θ than the curvature of eq. (3.22) near θ_0, which we have argued is strictly incorrect in many cases.

Chapter Four

Automated Polarization Rotation for Multi-Axis Rotational-Anisotropy Second Harmonic Generation Experiments

Chapter Five

Second harmonic generation as a probe of broken mirror symmetry in 1T-TaS_2

Chapter Six

Light-induced reorientation transition in the antiferromagnetic semiconductor $CaMn_2Bi_2$

Chapter Seven

Amplitude-mode electromagnon in the XXZ chain $CuBr_2$

Chapter Eight

Concluding remarks

*

Bibliography

[1] A. Alexandradinata, N. P. Armitage, Andrey Baydin, Wenli Bi, Yue Cao, Hitesh J. Changlani, Eli Chertkov, Eduardo H. da Silva Neto, Luca Delacretaz, Ismail El Baggari, G. M. Ferguson, William J. Gannon, Sayed Ali Akbar Ghorashi, Berit H. Goodge, Olga Goulko, G. Grissonnanche, Alannah Hallas, Ian M. Hayes, Yu He, Edwin W. Huang, Anshul Kogar, Divine Kumah, Jong Yeon Lee, A. Legros, Fahad Mahmood, Yulia Maximenko, Nick Pellatz, Hryhoriy Polshyn, Tarapada Sarkar, Allen Scheie, Kyle L. Seyler, Zhenzhong Shi, Brian Skinner, Lucia Steinke, K. Thirunavukkuarasu, Thaís Victa Trevisan, Michael Vogl, Pavel A. Volkov, Yao Wang, Yishu Wang, Di Wei, Kaya Wei, Shuolong Yang, Xian Zhang, Ya-Hui Zhang, Liuyan Zhao, and Alfred Zong.
The Future of the Correlated Electron Problem, July 2022.
arXiv:2010.00584 [cond-mat].

[2] Klaus-Dieter Bauer and Kurt Hingerl.
Bulk quadrupole contribution to second harmonic generation from classical oscillator model in silicon.
Opt. Express, 25(22):26567, October 2017.
doi: 10.1364/OE.25.026567.

[3] Robert R. Birss.
Symmetry and Magnetism.
North-Holland Pub. Co., 1964.

[4] Robert Boyd.
Nonlinear Optics.
Academic Press, third edition, mar 2008.

[5] Branton J. Campbell, Harold T. Stokes, David E. Tanner, and Dorian M. Hatch.
ISODISPLACE : a web-based tool for exploring structural distortions.
J Appl Crystallogr, 39(4):607–614, August 2006.
doi: 10.1107/S0021889806014075.

[6] Wikipedia contributors.
List of space groups — Wikipedia, the free encyclopedia, 2024.
[Online; accessed 06-March-2024].

[7] N.A.C. Cressie.
Statistics for Spatial Data.
A Wiley-interscience publication. J. Wiley, 1991.

[8] Pierre Curie.
Sur la symétrie dans les phénomènes physiques, symétrie d'un champ électrique et d'un champ magnétiqueu.
J. Phys. Theor. Appl., 3(1):393–415, 1894.

[9] F.M. Dekking, C. Kraaikamp, H.P. Lopuhaä, and L.E. Meester.
A Modern Introduction to Probability and Statistics: Understanding Why and How.
Springer Texts in Statistics. Springer London, 2006.

[10] M. Fiebig, D. Fröhlich, Th. Lottermoser, V. V. Pavlov, R. V. Pisarev, and H.-J Weber.
Second Harmonic Generation in the Centrosymmetric Antiferromagnet NiO.
Phys. Rev. Lett., 87(13):137202, September 2001.
doi: 10.1103/PhysRevLett.87.137202.

[11] J. W. Harter, L. Niu, A. J. Woss, and D. Hsieh.
High-speed measurement of rotational anisotropy nonlinear optical harmonic generation using position-sensitive detection.
Opt. Lett., 40(20):4671, October 2015.
doi: 10.1364/OL.40.004671.

[12] John David Jackson.
Classical electrodynamics.
Wiley, New York, NY, 3rd ed. edition, 1999.

[13] T.W.B Kibble and G.R Pickett.
Introduction. Cosmology meets condensed matter.
Phil. Trans. R. Soc. A., 366(1877):2793–2802, August 2008.
doi: 10.1098/rsta.2008.0098.

[14] Challa S.S.R. Kumar, editor.
Magnetic Characterization Techniques for Nanomaterials.
Springer Berlin Heidelberg, Berlin, Heidelberg, 2017.
doi: 10.1007/978-3-662-52780-1.

[15] Kenneth Levenberg.
A method for the solution of certain non-linear problems in least squares.
Quart. Appl. Math., 2(2):164–168, 1944.
doi: 10.1090/qam/10666.

[16] Donald W. Marquardt.
An Algorithm for Least-Squares Estimation of Nonlinear Parameters.
Journal of the Society for Industrial and Applied Mathematics, 11(2):431–441, June 1963.
doi: 10.1137/0111030.

[17] Aaron Meurer, Christopher P. Smith, Mateusz Paprocki, Ondřej Čertík, Sergey B. Kirpichev, Matthew Rocklin, AMiT Kumar, Sergiu Ivanov, Jason K. Moore, Sartaj Singh, Thilina Rathnayake, Sean Vig, Brian E. Granger, Richard P. Muller, Francesco Bonazzi, Harsh Gupta, Shivam Vats, Fredrik Johansson, Fabian Pedregosa, Matthew J. Curry, Andy R. Terrel, Štěpán Roučka, Ashutosh Saboo, Isuru Fernando, Sumith Kulal, Robert Cimrman, and Anthony Scopatz.
Sympy: symbolic computing in python.
PeerJ Computer Science, 3:e103, January 2017.
doi: 10.7717/peerj-cs.103.

[18] K Morey, Bryan T. Fichera, Baiqing Lv, Zongqi Shen, and Nuh Gedik.
Automated polarization rotation for multi-axis rotational-anisotropy second harmonic generation experiments.
In preparation.

[19] J. A. Nelder and R. Mead.
A Simplex Method for Function Minimization.
The Computer Journal, 7(4):308–313, January 1965.
doi: 10.1093/comjnl/7.4.308.

[20] Franz Neumann.
Vorlesungen über die Theorie der Elasticität der festen Körper und des Lichtäthers, gehalten an der Universität Königsberg.
Leipzig, B. G. Teubner, 1885.

[21] Shyue Ping Ong, William Davidson Richards, Anubhav Jain, Geoffroy Hautier, Michael Kocher, Shreyas Cholia, Dan Gunter, Vincent L. Chevrier, Kristin A. Persson, and Gerbrand Ceder.
Python Materials Genomics (pymatgen): A robust, open-source python library for materials analysis.
Computational Materials Science, 68:314–319, February 2013.
doi: 10.1016/j.commatsci.2012.10.028.

[22] Shreyas Patankar, Liang Wu, Baozhu Lu, Manita Rai, Jason D. Tran, T. Morimoto, Daniel E. Parker, Adolfo G. Grushin, N. L. Nair, J. G. Analytis, J. E. Moore, J. Orenstein, and D. H. Torchinsky.
Resonance-enhanced optical nonlinearity in the Weyl semimetal TaAs.
Phys. Rev. B, 98(16):165113, October 2018.
doi: 10.1103/PhysRevB.98.165113.

[23] P. S. Pershan.
Nonlinear Optical Properties of Solids: Energy Considerations.
Phys. Rev., 130(3):919–929, May 1963.
doi: 10.1103/PhysRev.130.919.

[24] G. D. Powell, J.-F. Wang, and D. E. Aspnes.
Simplified bond-hyperpolarizability model of second harmonic generation.
Physical Review B, 65(20), May 2002.
doi: 10.1103/PhysRevB.65.205320.

[25] Richard C. Powell.
Symmetry, Group Theory, and the Physical Properties of Crystals.
Springer New York, NY, 2010.

[26] William H. Press, Saul A. Teukolsky, William T. Vetterling, and Brian P. Flannery.
Numerical Recipes 3rd Edition: The Art of Scientific Computing.
Cambridge University Press, 3 edition, 2007.

[27] A. Ron, E. Zoghlin, L. Balents, S. D. Wilson, and D. Hsieh.
Dimensional crossover in a layered ferromagnet detected by spin correlation driven distortions.
Nat Commun, 10(1):1654, December 2019.
doi: 10.1038/s41467-019-09663-3.

[28] D. Sa, R. Valentí, and C. Gros.
A generalized Ginzburg-Landau approach to second harmonic generation.
Eur. Phys. J. B, 14(2):301–305, March 2000.
doi: 10.1007/s100510050133.

[29] H. T. Stokes, D. M. Hatch, and B. J. Campbell.
Isodistort.

[30] Darius H. Torchinsky, Hao Chu, Tongfei Qi, Gang Cao, and David Hsieh.
A low temperature nonlinear optical rotational anisotropy spectrometer for the determination of crystallographic and electronic symmetries.
Review of Scientific Instruments, 85(8):083102, August 2014.
doi: 10.1063/1.4891417.

[31] Pauli Virtanen, Ralf Gommers, Travis E. Oliphant, Matt Haberland, Tyler Reddy, David Cournapeau, Evgeni Burovski, Pearu Peterson, Warren Weckesser, Jonathan Bright, Stéfan J. van der Walt, Matthew Brett, Joshua Wilson, K. Jarrod Millman, Nikolay Mayorov, Andrew R. J. Nelson, Eric Jones, Robert Kern, Eric Larson, C J Carey, İlhan Polat, Yu Feng, Eric W. Moore, Jake VanderPlas, Denis Laxalde, Josef Perktold, Robert Cimrman, Ian Henriksen, E. A. Quintero, Charles R. Harris, Anne M. Archibald, Antônio H. Ribeiro, Fabian Pedregosa, Paul van Mulbregt, and SciPy 1.0 Contributors.
SciPy 1.0: Fundamental Algorithms for Scientific Computing in Python.

Nature Methods, 17:261–272, 2020.
doi: 10.1038/s41592-019-0686-2.

[32] H. Wackernagel.
Multivariate Geostatistics: An Introduction with Applications.
Springer Berlin Heidelberg, 2003.

[33] David J. Wales and Jonathan P. K. Doye.
Global Optimization by Basin-Hopping and the Lowest Energy Structures of Lennard-Jones Clusters Containing up to 110 Atoms.
J. Phys. Chem. A, 101(28):5111–5116, July 1997.
doi: 10.1021/jp970984n.

[34] Liang Wu, S. Patankar, T. Morimoto, N. L. Nair, E. Thewalt, A. Little, J. G. Analytis, J. E. Moore, and J. Orenstein.
Giant anisotropic nonlinear optical response in transition metal monopnictide Weyl semimetals.
Nature Phys, 13(4):350–355, April 2017.
doi: 10.1038/nphys3969.

[35] Y Xiang, D.Y Sun, W Fan, and X.G Gong.
Generalized simulated annealing algorithm and its application to the Thomson model.
Physics Letters A, 233(3):216–220, August 1997.
doi: 10.1016/S0375-9601(97)00474-X.